# Subtle tuning of micro-environment in COFs nanoribbons actuates low electricity-consumption photo-assisted Co-electrolysis of methanol and CO2

Yi-Rong Wang[1,§], Hui-Min Ding[1,§], Ming Yue[1,§], Qi Li[1], Jing-wen Shi[1], Qing Huang[2], Jie Zhou[3], Ying Zang[1] (✉), Yifa Chen[1] (✉), Shun-Li Li[1], and Ya-Qian Lan[1] (✉)

[1] *Guangdong Provincial Key Laboratory of Carbon Dioxide Resource Utilization, School of Chemistry, South China Normal University, Guangzhou 510006, China*

[2] *College of Materials Science and Engineering, Nanjing Forestry University, Nanjing 210037, China*

[3] *Key Laboratory of Electrochemical Energy Storage and Energy Conversion of Hainan Province, School of Chemistry and Chemical Engineering, Hainan Normal University, Haikou 571158, China*

[§] *Yi-Rong Wang, Hui-Min Ding, and Ming Yue contributed equally to this work.*

## ABSTRACT

The lower electricity consumption (EC) and higher value-added products are much desired yet still challenging for the development of $CO_2$ coupling electrocatalytic systems. Herein, we give insight into the inherent nature of the retrenchment of EC by exploring the photo-assisted co-electrolysis of methanol and $CO_2$ system using a kind of hydroxyl-rich covalent organic frameworks (Dha-COF-Co) with well-tuned pore structure and morphology. Specifically, the hydroxyl induced hydrogen bond interaction in Dha-COF-Co enables to simultaneously regulate the pore microenvironment and nanoribbon morphology of COFs for performance boosting. Notably, the obtained Dha-COF-Co nanoribbon exhibits an overall EC retrenchment of ~41.2% (highest in porous crystalline materials to date) when replacing the anodic OER with MOR in the photo-electrocatalytic MOR-$CO_2$RR coupling system, as well as superior $FE_{HCOOH}$ (anode, ~100%) and $FE_{CO}$ (cathode, >95%) at 1.8 V. Combined theoretical calculations with various characterizations, the vital role of hydroxyl group in both microenvironment and morphology tuning that can facilitate the $CO_2$RR and MOR kinetics to retrench the EC has been intensively discussed.

## 1 Introduction

The capture, conversion, and utilization of $CO_2$ have become urgent issues to be solved in the context of "carbon neutrality" policy [1–3]. In particular, electrocatalytic $CO_2$ reduction reaction ($CO_2$RR), powered by renewable electricity, offers potential for energy storage and artificial closure of carbon cycle under mild conditions [4–13]. However, the conventional anodic oxygen evolution reaction (OER, theoretical oxidation potential of 1.23 V vs. RHE) coupled to $CO_2$RR reaction consumes up to 90% of the electricity while producing low valuable oxygen (a near-infinite resource in atmosphere) [14–22]. This thermodynamic constrain results in high electricity consumption (EC), and henceforth unsatisfied economic efficiency in $CO_2$RR-OER coupling system [23]. In order to improve the economic feasibility of $CO_2$RR, it is much essential to lower the overall EC for $CO_2$ coupling electrocatalytic systems.

For $CO_2$ coupling electrocatalytic systems, there are some possible strategies for lowering the EC, including the replacing OER with more thermodynamically favored half reactions, introducing advanced assisted techniques (e.g., light energy, heat energy or magnetic energy) or improving the reaction kinetics of electrocatalysts, etc. Initially, utilizing new anodic oxidation reactions that are more thermodynamically favorable than OER could be an effective strategy to be paired with cathodic half reaction ($CO_2$RR) for radically lowering the EC and improving the energy conversion efficiency of the overall electrolysis [24–32]. Specifically, methanol oxidation reaction (MOR) is a potential anodic reaction to be coupled with $CO_2$RR, in which methanol can be transformed to value-added chemicals such as formic acid

Address correspondence to Ying Zang, yzang0717@163.com; Yifa Chen, chyf927821@163.com; Ya-Qian Lan, yqlan@m.scnu.edu.cn

and thus might reduce the overall cost and increase economic efficiency [33–36]. In addition to this, the photo-electrocatalytic method has been recognized as a promising approach to realize high selectivity in MOR and $CO_2RR$ under mild conditions [37–39]. The light sensitive electrocatalysts would change the electronic property and thus the activity toward MOR and $CO_2RR$ when coupled with photon energy under light irradiation, eventually lowering EC and improving energy conversion efficiency. Based on these issues, the kinetics of MOR and $CO_2RR$ are also key factors that dominate the EC of MOR-$CO_2RR$ coupling system, during which the faster kinetics enable a lower cell potential and meanwhile lower EC [40–42]. Therefore, the design of efficient $CO_2$ coupling electrocatalytic systems that can simultaneously meet these requirements to achieve lower EC and higher value-added products are much desired.

With these considerations in mind, the design of efficient electrocatalysts would play a vital role in achieving such powerful $CO_2$ coupling electrocatalytic systems. Specifically, there are some basic demands for the design of target photo-electrocatalytic MOR-$CO_2RR$ electrocatalysts: 1) active sites for the boosted kinetics of both MOR and $CO_2RR$; 2) unique structure struts for efficient light absorption and photoelectron conversion and 3) catalytic microenvironment tuning and optimization for structure-property relationship and mechanism study. Nevertheless, the reported works for MOR-$CO_2RR$ coupling systems are mostly focused on the selectivity improvement by changing catalyst structure, whereas some important strategies, like the tuning of microenvironment or morphology, introducing auxiliary units and regulating inherent photo-electronic property have been rarely explored. In this regard, covalent organic frameworks (COFs), possessing unique properties like abundant channels, clear crystalline structures, high stability and adjustability, are regarded as ideal platform for photo-electrocatalytic MOR-$CO_2RR$ coupling system [43–45]. Especially attractive are their benefits in specially designed structure and tunability that may impart COFs with well-tuned microenvironments for kinetic improvement, integration with advanced assisted techniques and mechanism research. Therefore, it would be very interesting to explore the effect of microenvironment on morphology, performance boosting and catalytic mechanism to investigate the probability of COFs in low EC photo-electrocatalytic MOR-$CO_2RR$ coupling system.

Herein, we give insight into the inherent nature of the retrenchment of EC by exploring the photo-electrocatalytic MOR-$CO_2RR$ coupling system using a kind of hydroxyl-rich COFs (Dha-COF-Co) with well-tuned pore structure and morphology (Scheme 1). The hydroxyl-rich COFs nanoribbons (Dha-COF-M (M = Co, Ni and H)) were selected as the model catalysts to investigate the photo-electrocatalytic MOR coupled with $CO_2RR$, during which they serve as the bifunctional catalysts can simultaneously accomplish the efficient photo-electrocatalytic MOR and $CO_2RR$ in an integrated system. Notably, an overall EC retrenchment of ~41.2% (highest in porous crystalline materials) can be achieved when replacing the anodic OER by MOR in the photo-electrocatalytic MOR-$CO_2RR$ coupling system for Dha-COF-Co, which can give a $FE_{HCOOH}$ (anode, ~100%) and $FE_{CO}$ (cathode, >95%) at 1.8 V and represent to be one of the highest performances to date. Moreover, the vital role of hydroxyl functional group that can accelerate the $CO_2RR$ and MOR kinetics has been systematically studied by DFT calculations and sufficient characterizations, in which the hydroxyl can act as the auxiliary catalytic site to boost the $H_2O$ dissociation of MOR reaction and

facilitate mass transfer. This work offers a new design strategy of COFs to lower the EC and improve the energy efficiency of photo-electrocatalytic MOR-$CO_2RR$ coupling system.
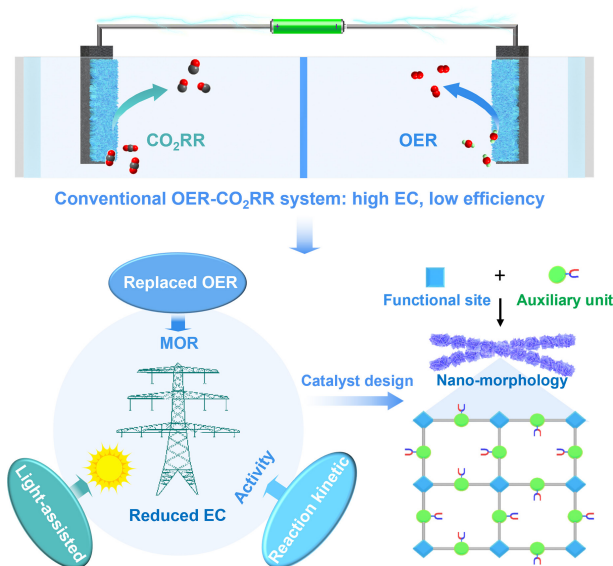


**Scheme 1** The schematic illustration of low electricity consumption (EC) photo-electrocatalytic MOR-$CO_2RR$ coupling system.

## 2 Experimental

### 2.1 Materials

All chemicals and solvents were commercially available and used without further purification. Potassium bicarbonate ($KHCO_3$), potassium hydroxide (KOH), methanol, acetonitrile, N-butyl alcohol, ethanol, 1, 2-dichlorobenzene, chloroform, acetic acid, N, N-dimethylformamide (DMF) and N, N-dimethylacetamide (DMA) were purchased from China National Medicines Corporation Ltd. Nafion solution (5 wt.%) were obtained from Sigma-Aldrich. Cobalt acetate tetrahydrate ($Co(OAc)_2 \cdot 4H_2O$) and nickel acetate tetrahydrate ($Ni(OAc)_2 \cdot 4H_2O$) were obtained from Shanghai Aladdin Bio-Chem Technology Co., Ltd. 2,3-dihydroxynaphthalene-1,4-dicarbaldehyde, tetrakis(4-aminophenyl)-porphinato and naphthalene-1,4-dicarboxaldehyde were purchased from Jilin Chinese Academy of Sciences-Yanshen Technology Co., Ltd. Carbon paper was purchased from Fuel Cell Store. All aqueous solutions were prepared with Millipore water (18.25 MΩ).

### 2.2 Synthesis of Dha-COF-Co

TAPP-Co (14.7 mg, 0.02 mmol), 2,3-dihydroxynaphthalene-1,4-dicarbaldehyde (8.7 mg, 0.04 mmol), 1,2-dichlorobenzene (0.33 mL), N,N-dimethylacetamide (1.0 mL) and 6 M aqueous acetic acid (0.2 mL) were mixed in a Pyrex tube (o.d. × length, 19 cm × 65 mm). After sonication for about 20 min, the tube was flash frozen at 77 K (liquid $N_2$ bath) and degassed to achieve an internal pressure of ~100 mTorr. After the temperature recovers to room temperature, the mixture was heated at 120 °C and left undisturbed for 72 h. After cooling to room temperature, the precipitate was filtered and washed thoroughly with THF and acetone each for three times. After filtration, the wet sample was transferred to a Soxhlet extractor and washed with THF (24 h). Finally, the product was evacuated at 120 °C under dynamic

vacuum overnight to yield activated sample. Other preparation of the samples as well as the testing of the properties is described in detail in the Electronic Supplementary Material (ESM).

## 3    Results and discussion

### 3.1    Synthesis and characterization

Dha-COF-M (M = Co, Ni and H) were synthesized by Schiff-base condensation of 2,3-dihydroxynaphthalene-1,4-dicarbaldehyde (Dha) and metallized 5,10,15,20-tetrakis (4-aminophenyl)-porphinato (TAPP-M, M = Co, Ni and H) through a solvothermal strategy (Fig. 1(a)). The crystalline structure of Dha-COF-Co was defined by a combined method using powder X-ray diffraction (PXRD) and theoretical structural simulations on Materials Studio (Fig. 1(b) and Fig. S1 in the ESM). The results give a unit cell parameter ($a = b = 33.0663$ Å, $c = 3.8831$ Å, $\alpha = \beta = \gamma = 90°$) that complies with the $P4$ space group using AA stacking mode, which is supported by the difference plot with unweighted-profile $R$ factor ($R_p$) of 1.62% and weighted profile $R$ factor ($R_{wp}$) of 2.19% (Fig. 1(b) and Table S1 in the ESM). The intense peaks at 3.52°, 5.00°, 5.58°, and 7.06° in the PXRD pattern can be attributed to the (1 0 0), (2 0 0), (2 1 0) and (2 2 0) facets of Dha-COF-Co, respectively. The simulated crystal structure shows that there is a pore channel along the c axis with a theoretical pore size of 1.96 nm, and the distance between adjacent stacking 2D sheets is 3.88 Å (Fig. 1(a)). Furthermore, the PXRD patterns of Dha-COF-H/Ni also show high crystallinity (Figs. S2 and S3 in the ESM). The chemical structures of Dha-COF-M (M = Co, Ni and H) have

been further confirmed by FT-IR spectra. In the FT-IR spectra, a new characteristic peak at 1622 cm⁻¹ attributed to the C=N stretching vibration is observed in Dha-COF-Co, while the C=O stretching vibration (1700 cm⁻¹) and -NH₂ vibration (3200–3500 cm⁻¹) in monomers are nearly disappeared (Fig. S4 in the ESM) [46]. Besides, compared with TAPP, the new peak of Co-N stretching vibration at 999 cm⁻¹ and disappeared peak of N-H stretching vibration at 3315 cm⁻¹ in Dha-COF-Co indicate the metal coordination at the porphyrin center (Fig. S4 in the ESM) [47]. These results confirm the successful preparation of Dha-COF-M (M = Co, Ni and H).

The surface area and porosity of samples were examined by N₂ sorption measurement at 77 K (Fig. 1(c) and Fig. S5 in the ESM). The Brunauer-Emmett-Teller surface area ($S_{BET}$) and total pore volume ($V_t$) of Dha-COF-Co are calculated to be 525 m²·g⁻¹ and 0.65 cm³·g⁻¹, respectively (Fig. 1(c)). As a comparison, the $S_{BET}$ and $V_t$ of Dha-COF-Ni (494 m²·g⁻¹, 0.63 cm³·g⁻¹) are close to that of Dha-COF-Co (Fig. S5 in the ESM). The pore size for Dha-COF-M (M = Co and Ni) is in conformity with the theoretical results (Fig. 1(c) and Fig. S5 in the ESM). In addition, CO₂ adsorption tests have been performed to analyze the CO₂ capture ability of Dha-COF-M (M = Co, Ni) (Figs. S6 and S7 in the ESM). The CO₂ uptake capacity of Dha-COF-Co are 38 cm³·g⁻¹ at 273 K and 24 cm³·g⁻¹ at 298 K, higher than the values of Dha-COF-Ni (34 cm³·g⁻¹, 273 K; 18 cm³·g⁻¹, 298 K) (Figs. S6 and S7 in the ESM). Moreover, the stability of sample is crucial for its further application. Different solvent conditions (i.e., mixed solution of 1 M KOH and 1 M methanol, and 0.5 M KHCO₃ solution) were used to verify the chemical stability of samples through an immersion process at room temperature for at least 12 h. No obvious change in the PXRD patterns can be observed after testing, indicating the well-maintained crystalline structure and superior chemical stability of Dha-COF-Co (Figs. S8 and S9 in the ESM).

In addition, the morphology of Dha-COF-Co has been characterized by transmission electron microscopy (TEM), which displays nanoribbon morphology (Fig. 1(d) and Fig. S10 in the ESM). The structural characteristics of Dha-COF-Co have been visualized by high-resolution transmission electron microscopy (HRTEM). Dha-COF-Co displays clear crystalline lattice plane, confirming its high crystallinity (Fig. 1(d)). To get deep insight into the possible morphology formation mechanism, the PXRD and TEM tests of intermediates at various reaction time were performed (Figs. S11 and S12 in the ESM). The PXRD results clearly show increased crystallinity with reaction proceeding, during which the peaks of Dha-COF-Co emerge at 12 h and gradually strengthen when the reaction time prolongs to 72 h (Fig. S11 in the ESM). The TEM tests show that Dha-COF-Co displays short nanoribbon morphology at 6 h. After that, the surface of nanoribbon becomes rough and the nanoribbon grows longer to the final state at 72 h. Besides, Naph-COF-Co (without hydroxyl group compared with Dha-COF-Co) was also prepared and tested as comparison (Figs. S13 and S14 in the ESM). In sharp contrast, the TEM tests exhibit that Naph-COF-Co displays the nanosphere morphology during all of the reaction time (Fig. S14 in the ESM). These results prove the vital role of hydroxyl group in directing the morphology tuning into nanoribbons, meanwhile the existed abundant hydroxyl groups might also adjust the microenvironment of Dha-COF-Co that is favourable for the electro-catalytic applications.

Besides, the scanning transmission electron microscopy (STEM) with energy-dispersive X-ray spectrum (EDS)
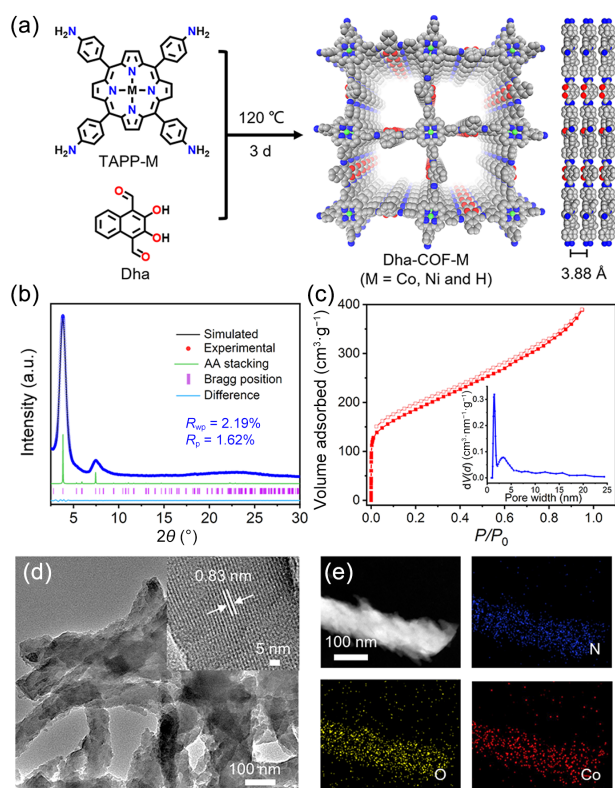


**Figure 1**    Preparation and characterization of Dha-COF-M (M = Co, Ni and H). (a) Schematic illustration of the preparation protocol of Dha-COF-M (M = Co, Ni and H). (b) Experimental and simulated PXRD patterns of Dha-COF-Co. (c) N₂ sorption curves of Dha-COF-Co at 77 K (inset shows the pore-size distribution profile). (d) TEM image of Dha-COF-Co (insert is the HRTEM image). (e) STEM and elemental mapping images of Dha-COF-Co.

demonstrate that C, N, O, and Co elements are uniformly distributed over Dha-COF-Co (Fig. 1(e)) and Fig. S18 in the ESM). Additionally, Ni is also uniformly distributed over Dha-COF-Ni (Fig. S15 in the ESM). X-ray photoelectron spectroscopy (XPS) was conducted to investigate the chemical states of the existed elements in Dha-COF-M (M = Co, Ni). In the XPS spectrum of Co 2p for Dha-COF-Co, the binding energy at 795.6 and 780.2 eV are attributed to Co (II) (Fig. S16 in the ESM) [48]. For Dha-COF-Ni, Ni is also divalent from XPS results (Fig. S17 in the ESM) [49]. The metal contents in Dha-COF-Co and Dha-COF-Ni were determined to be 4.46% and 4.31% by inductively coupled plasma optical emission spectrometry (ICP-OES).

## 3.2 Electrochemical performance

Initially, the electrocatalytic performances of Dha-COF-M (M = Co, Ni and H) were carried out in a H-type cell for $CO_2RR$, MOR and OER, respectively. The liquid products were monitored by $^1H$ nuclear magnetic resonance ($^1H$ NMR) and ion chromatography (IC). Meanwhile, the gas products were monitored and quantified by gas chromatography (GC). Compared with the linear sweep voltammetry (LSV) curve of Dha-COF-Co in Ar-saturated 0.5 M $KHCO_3$ solution, the LSV curve in $CO_2$-saturated 0.5 M $KHCO_3$ solution shows higher current density and smaller onset potential, indicating that $CO_2RR$ is more likely to occur at the cathode rather than HER (Fig. S19 in the ESM). Additionally, the total current density at –1.1 V of Dha-COF-Ni (–8.1 mA·cm$^{-2}$) and Dha-COF-H (–4.5 mA·cm$^{-2}$) are lower than Dha-COF-Co (–33.6 mA·cm$^{-2}$), indicating a better $CO_2RR$ activity of Dha-COF-

Co (Fig. 2(a)). Similarly, the OER and MOR performances of Dha-COF-M (M = Co, Ni and H) were measured by LSV curves at the anode in both 1 M KOH and mixed solution of 1 M KOH and 1 M methanol, respectively. The current density of Dha-COF-Co increases remarkably in presence of MOR, and the potential required (1.38 V at 10 mA·cm$^{-2}$) is 350 mV lower than that of OER (Fig. S20 in the ESM). In comparison, Dha-COF-Ni and Dha-COF-H require potentials of 1.39 and 1.71 V, respectively, to achieve the current density of 10 mA·cm$^{-2}$ in MOR (Fig. 2(b)). Besides, the reaction kinetics of Dha-COF-Co for MOR and OER were estimated by the Tafel plots (Fig. S21 in the ESM). The calculated Tafel slope of MOR (34.1 mV·dec$^{-1}$) is much smaller than that of OER (57.9 mV·dec$^{-1}$). The above results suggest that MOR is a more favorable anodic reaction than OER.

To evaluate the activity and selectivity of Dha-COF-M (M = Co, Ni and H) for $CO_2RR$ and MOR, the Faradaic efficiency (FE) of products under controlled potential have been quantified by GC and IC tests. CO and $H_2$ are shown to be the main products for $CO_2RR$ and no liquid product is detected (Figs. S22 and S23 in the ESM). HCOOH is the primary product for MOR (Fig. S24 in the ESM). The $FE_{CO}$ of Dha-COF-Co can reach up to 82.1±3.4% at –0.9 V, and $FE_{HCOOH}$ of Dha-COF-Co keeps higher than 91% over the potential range from 1.4 to 1.5 V, demonstrating an obviously high activity for the conversion of $CO_2$ to CO and methanol to HCOOH (Figs. 2(c) and 2(d)). In contrast, the highest $FE_{CO}$ and $FE_{HCOOH}$ of Dha-COF-Ni are 70.2±2.2% (at –0.9 V) and 89.0±1.9% (at 1.4 V), respectively (Figs. 2(c) and 2(d)). Besides, Dha-COF-H has no $CO_2RR$ activity, whereas it can convert methanol to HCOOH with the maximum FE of 48.9±2.0% (at 1.6 V) (Figs. 2(c) and 2(d)). Additionally, some contrast experiments have been conducted to indicate the sources of catalytic activity for Dha-COF-Co. The results imply that the bare carbon paper and other additives (acetylene black (AB) and Nafion) have no $CO_2RR$ and MOR activity (Figs. S25 and S26 in the ESM). Moreover, Naph-COF-Co, as a none hydroxyl counterpart of Dha-COF-Co, displays $FE_{CO}$ and $FE_{HCOOH}$ of 74.3±3.2% (–1 V) and 70.9±1.5% (1.5 V), respectively (Fig. S27 in the ESM). The above results suggest that the catalytic active site of $CO_2RR$ is porphyrin-Co, meanwhile the porphyrin-Co and hydroxyl group might play synergistic role in enhancing the catalytic activity of MOR.

In addition, the partial current density at applied potentials of sample is calculated to study the excellent activity for MOR and $CO_2RR$. Dha-COF-Co displays high partial HCOOH and CO current density of 12.7 mA·cm$^{-2}$ (at 1.6 V) and –11.3 mA·cm$^{-2}$ (at –1.1 V), respectively (Fig. S28 in the ESM). The partial HCOOH and CO current density of Dha-COF-Co is higher than that of Dha-COF-Ni and Dha-COF-H, indicating the superior activity of Dha-COF-Co in $CO_2RR$ and MOR (Fig. S28 in the ESM). Moreover, electrochemical impedance spectroscopy of Dha-COF-Co was tested to understand the kinetics of $CO_2RR$ and MOR on electrode/electrolyte interface (Fig. S29 in the ESM). As shown in the Nyquist plots, Dha-COF-Co has smaller charge transfer resistance ($R_{ct}$) in $CO_2RR$ (40.7 Ω) and MOR (38.7 Ω) than that of Dha-COF-Ni ($CO_2RR$, 65.4 Ω and MOR, 70.2 Ω), confirming the faster electron transfer on Dha-COF-Co, thus enhancing the reaction kinetics. Additionally, the $R_{ct}$ for Dha-COF-Co in OER (129.3 Ω) is much larger than that in MOR (38.7 Ω), indicating a faster electron transfer process in MOR. In order to confirm the carbon source of products for MOR and $CO_2RR$, isotopic experiments under identical reaction conditions were carried out using $^{13}CH_3OH$ and $^{13}CO_2$ as the substrate in the anode and
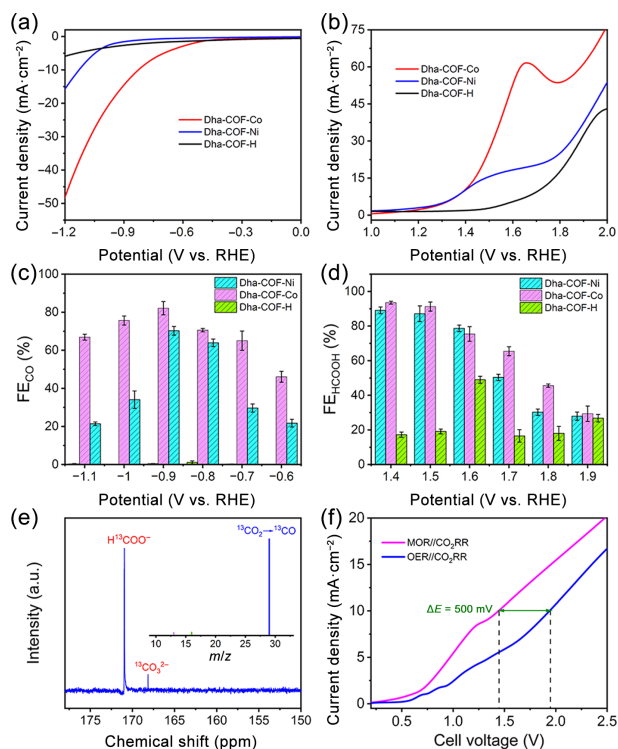


**Figure 2** Electrocatalytic performance of Dha-COF-M (M = Co, Ni and H). (a) LSV curves of Dha-COF-M (M = Co, Ni and H) at cathode in 0.5 M $KHCO_3$. (b) LSV curves of Dha-COF-M (M = Co, Ni and H) at anode in 1 M KOH and 1 M methanol mixed solution. (c) $FE_{CO}$ at different applied potentials of Dha-COF-M (M = Co, Ni and H). (d) $FE_{HCOOH}$ at different applied potentials of Dha-COF-M (M = Co, Ni and H). (e) $^{13}C$ NMR spectrum and mass spectrum of MOR and $CO_2RR$ product in isotopic tests. (f) Cell LSV curves of MOR∥$CO_2RR$ and OER∥$CO_2RR$ using Dha-COF-Co as both anode and cathode catalysts.

cathode. The $^{13}C$ NMR spectrum of anodic product shows peaks at about 171.0 ppm and 168.1 ppm, which can be assigned to $HCOO^-$ and $CO_3^{2-}$, respectively. The gas chromatography-mass spectrometry (GC-MS) detects that the *m/z* values of products are 13, 16, 29, corresponding to $^{13}C$, $^{16}O$ and $^{13}CO$, respectively (Fig. 2(e)). These evidences explicitly demonstrate the origination of oxidation and reduction products of MOR and $CO_2RR$ from the $CH_3OH$ and $CO_2$, respectively, proving the high performance of Dha-COF-Co.

Inspired by the excellent $CO_2RR$ and MOR performance of Dha-COF-Co, co-electrolysis of $CO_2$ and methanol (denoted as MOR||$CO_2RR$) in two-electrode system was performed. The LSV of two-electrode system confirmed the benefit of anodic MOR in lowering the overall cell voltage (Fig. 2(f)). For Dha-COF-Co, the MOR||$CO_2RR$ only needs 1.44 V cell voltage to deliver a current density of 10 mA·cm$^{-2}$, which is 500 mV lower than that of OER||$CO_2RR$. In addition, although the performance is not as good as that of Dha-COF-Co, Dha-COF-Ni also shows much lower cell voltage (1.85 V) in MOR||$CO_2RR$ system than OER||$CO_2RR$ system (2.43 V) at the current density of 10 mA·cm$^{-2}$, indicating the superiority of MOR||$CO_2RR$ system (Fig. S30 in the ESM). To verify the electrocatalytic MOR and $CO_2RR$ performance of sample in the two-electrode system, the oxidation and reduction products were separately collected and the FE values were calculated. In comparison to OER||$CO_2RR$ cell ($FE_{CO}$ < 50%, Fig. S31 in the ESM), the $FE_{CO}$ of Dha-COF-Co is largely improved and can reach up to 90.0±0.7% at 1.9 V when MOR is coupled with $CO_2RR$ (Fig. S31 in the ESM). Meanwhile, at anodic MOR, a 90.8±0.8% $FE_{HCOOH}$ can be achieved at 1.8 V, and retains > 67% at all applied cell voltages (Fig. 3(a)). Similarly, Dha-COF-Ni displays the higher $FE_{HCOOH}$ (82.4±5.0%, 1.8 V) and

$FE_{CO}$ (77.7±4.9%, 1.8 V) of MOR||$CO_2RR$ than the system of OER||$CO_2RR$ (Fig. S32 in the ESM). Hence, the MOR-$CO_2RR$ coupling system will form serviceable high-valued products and increase the practicability of $CO_2$ conversion.

In addition to the electrocatalytic performance, Dha-COF-Co composed of porphyrin-Co unit possesses efficient light absorption and photoelectron conversion ability, which will alter its electronic properties under light irradiation and hold promise in reducing EC and improving energy efficiency when coupled with light energy (Fig. S33 in the ESM) [34, 42, 43, 46]. In view of these, we propose that light energy might accelerate the activity of MOR-$CO_2RR$ coupling system. Therefore, the MOR||$CO_2RR$ performance with light illumination is carried out in a two-electrode system. The photo-current test of Dha-COF-Co implies that the current density increases significantly with the assistance of light, supplying a satisfactory foundation for photo-electrocatalytic MOR-$CO_2RR$ coupling system. Specifically, compared with MOR||$CO_2RR$, the $FE_{HCOOH}$ of MOR||$CO_2RR$ with light improves to > 80% from 1.7 to 2.0 V cell voltage and achieves the highest value of 98.3±0.4% at 1.8 V (Figs. 3(c) and 3(d) and Table S2 in the ESM). Meanwhile, the corresponding $FE_{CO}$ can maintain above 82% in a broad voltage window (1.8 to 2.1 V), and the optimized value approaches to 95.9±1.5% at 1.9 V. In addition, for the COF-366-Co, the $FE_{CO}$ of MOR||$CO_2RR$ with light illumination reaches to the highest value of 70.7±0.8% at 2.3 V, meanwhile the corresponding $FE_{HCOOH}$ is close to 78.4±1.4% at 2.0 V (Fig. S34 in the ESM). Similarly, for the Naph-COF-Co, the $FE_{CO}$ of MOR||$CO_2RR$ with light illumination reaches to the highest value of 77.7±2.9% at 2.1 V, meanwhile the corresponding $FE_{HCOOH}$ is close to 79.3±1.3% at 1.9 V (Fig. S35 in the ESM). These comparison results sufficiently verify the importance of naphthalene and hydroxyl groups in boosting the overall efficiency of the coupling system.

EC, depending on the $j_{CO}$ value, is a key parameter to estimate the energy conversion efficiency of MOR-$CO_2RR$ coupling system [23, 42]. The result shows that the EC can be reduced by 12.5%−33.3% when MOR replaces OER at the anode (Fig. 3(e) and S36 in the ESM). In the photo-electrocatalytic MOR-$CO_2RR$ coupling system, the declined EC can reach up to 41.2%, which is highest among the porous crystalline materials to date (Fig. 3(e)) [23, 34, 42]. In principle, this could drastically reduce the cradle-to-gate $CO_2$ emissions and improve the economy of $CO_2RR$. The persistence of the catalytic performance is a vital element for estimating the practical applications of samples. Thus, the chronoamperometric test was carried out to reveal the stability of Dha-COF-Co in the two-electrode system. As displayed in Fig. 3(f), the catalytic performance of Dha-COF-Co can be maintained for 5 h at 1.8 V cell voltage with $FE_{HCOOH}$ over 90% and $FE_{CO}$ over 80%. Moreover, the post-mortem characterization (i.e., XPS test) was tested to prove the stability of Dha-COF-Co after electrochemical process. The results imply that the binding energy of Co species are consistent with the sample before catalytic test (Fig. S37 in the ESM). These results indicate that the Dha-COF-Co has excellent electrocatalytic stability. Based on the experiment result, EC is closely related to the replaced thermodynamically favored MOR, advanced assisted light energy and the improved reaction kinetics of electrocatalysts, which can be largely reduced through the overall system design in this work.

*In-situ* ATR-FTIR spectra have been conducted to investigate the intermediates during electrocatalytic process to further study the reaction mechanism (Figs. 4(a) and 4(b)). The signals at 1473 and 1030 cm$^{-1}$ in MOR spectrum are ascribed to $*CH_2O$ and
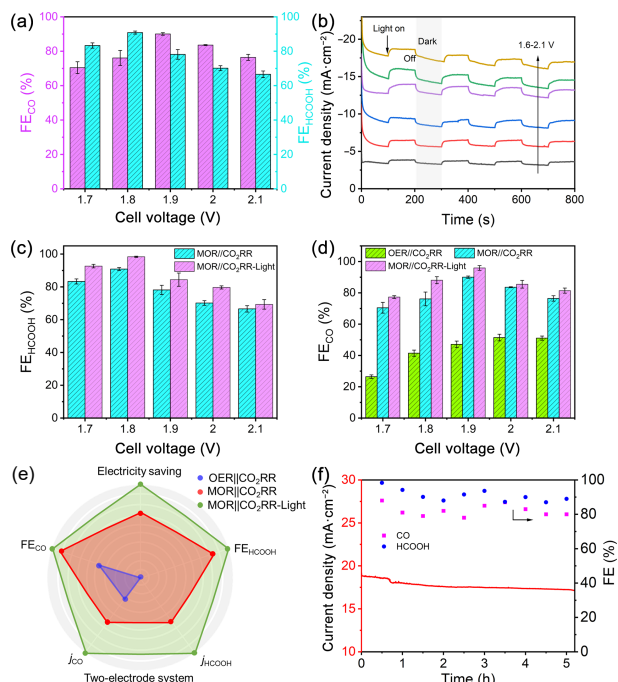


**Figure 3** MOR||$CO_2RR$ performance of Dha-COF-Co. (a) $FE_{CO}$ (cathode) and $FE_{HCOOH}$ (anode) of Dha-COF-Co for MOR||$CO_2RR$ at different potentials. (b) Photo-current curves of Dha-COF-Co. (c) $FE_{CO}$ (cathode) of Dha-COF-Co for OER||$CO_2RR$, MOR||$CO_2RR$ and MOR||$CO_2RR$ with light irradiation. (d) $FE_{HCOOH}$ (anode) of Dha-COF-Co for MOR||$CO_2RR$ and MOR||$CO_2RR$ with light irradiation. (e) Radar chart of the performances for photo-electrocatalytic MOR-$CO_2RR$ coupling system. (f) *I-t* test of Dha-COF-Co for MOR||$CO_2RR$ with light irradiation at 1.8 V.
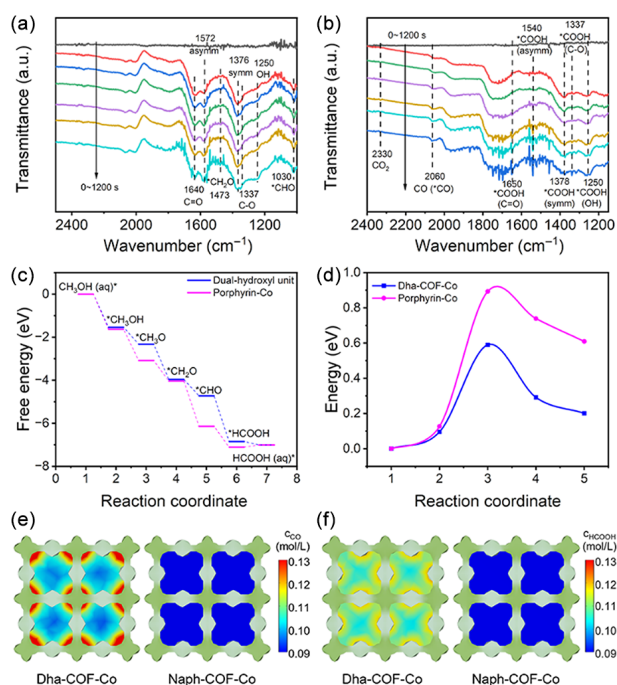
**Figure 4** *In-situ* ATR-FTIR spectra and DFT calculations of Dha-COF-Co. (a) *In-situ* ATR-FTIR spectra of Dha-COF-Co during the MOR process. (b) *In-situ* ATR-FTIR spectra of Dha-COF-Co during the CO$_2$RR process. (c) Free energy diagram of dual-hydroxyl and porphyrin-Co in Dha-COF-Co for MOR. The applied electrode potential is 1.4 V. (d) The energy barriers of hydrolysis dissociation proton reactions (H$_2$COH* + OH$^-$ →CH$_2$O* + H$_2$O + e$^-$) on porphyrin-Co and Dha-COF-Co. (e) The variation of CO concentration on the Dha-COF-Co and Naph-COF-Co obtained by FEM simulation at 1.5 V (the $c_{CO}$ is shown by colormap, the light green square represents the porphyrin-Co unit and the grey circle stands for dual-hydroxyl units). (f) The variation of HCOOH concentration on the Dha-COF-Co and Naph-COF-Co obtained by FEM simulation at 1.5 V (the $c_{HCOOH}$ is shown by colormap, the light green square represents the porphyrin-Co unit and the grey circle stands for dual-hydroxyl units).

*CHO, which are the key intermediates for HCOOH generation [50]. The peaks at 1640, 1572, 1376, 1337 and 1250 cm$^{-1}$ are attributed to C=O stretch, asymmetric stretch, symmetric stretch, C-O stretch and OH deformation of *HCOOH, respectively (Fig. 4(a)) [51]. Besides, in the CO$_2$RR spectrum, the bands appeared at 1650, 1540, 1378, 1337 and 1250 cm$^{-1}$ are assigned to C=O stretch, asymmetric stretch, symmetric stretch, C-O stretch and OH deformation of COOH*, respectively, which is a vital intermediate for CO$_2$RR to CO. The peak detected at 2060 cm$^{-1}$ is ascribed to the chemisorbed CO (*CO) (Fig. 4(b)) [51]. These crucial intermediates provide a solid foundation for further study of reaction mechanisms.

Based on above-mentioned results, density functional theory (DFT) calculations have further been performed to reveal the catalytic mechanism. There are two possible sites (i.e., dual-hydroxyl and porphyrin-Co units) in Dha-COF-Co for MOR and CO$_2$RR. Firstly, the free energy diagrams of MOR and CO$_2$RR are calculated based on dual-hydroxyl and porphyrin-Co units in Dha-COF-Co, respectively (Fig. 4(c), and Figs. S38–S43 in the ESM). The free energy diagram results show that the desorption of HCOOH (aq)* and generation of *COOH are rate-determining steps (RDS) for MOR and CO$_2$RR, respectively. The MOR activity of the dual-hydroxyl unit ($\Delta G^0_{max}$ = −0.159 eV) is better than that of porphyrin-Co unit ($\Delta G^0_{max}$ = 0.099 eV), while the CO$_2$RR activity of dual-hydroxyl unit ($\Delta G^0_{max}$ = 0.876 eV) is worse than that of porphyrin-Co ($\Delta G^0_{max}$ = 0.749 eV), which coincides with

the experimental data. Then, the energy barriers of hydrolysis dissociation proton reactions of porphyrin-Co units and Dha-COF-Co are calculated using nudged elastic band (NEB) simulation and H$_2$COH* + OH$^-$→CH$_2$O* + H$_2$O + e$^-$ is selected as the model reaction (Fig. 4(d)) [41]. From the results of NEB, it can be seen that the barrier decreases when dual-hydroxyl groups are presented, indicating that dual-hydroxyl groups can provide additional hydrogen bonding networks, making OH$^-$ stable and promoting the dissociation of H$_2$O to improve the reaction kinetics [52]. This is consistent with the previous conclusion on the oxygen reactivity of materials and the proton donating reaction activity of alkaline hydrolysis [52].

Additionally, to further reveal the cause of the improved activity, the differential charge density of HCOOH* adsorption on dual-hydroxyl and porphyrin-Co units in Dha-COF-Co are calculated (Fig. S44 in the ESM). The result shows that the charge migration is more apparent on porphyrin-Co unit. The high charge transfer often indicates a stronger bonding effect at the site, which means that porphyrin-Co has stronger adsorption ability for intermediates. The strength of intermediate adsorption has different effects on MOR and CO$_2$RR. For MOR, due to the desorption of HCOOH* is the RDS, the stronger adsorption will lead to a decrease in activity. While for CO$_2$RR, due to the formation of COOH* is the RDS, stronger adsorption will enhance its activity.

To gain a more accurate understanding of the involvement of porphyrin-Co and dual-hydroxyl groups in the coupling reaction, as well as to showcase the role of dual-hydroxyl groups, the circuit of the electrolysis process is simulated employing the finite element method (FEM). Dha-COF-Co and Naph-COF-Co (the none dual-hydroxyl counterpart of Dha-COF-Co) were selected as the structure platforms. The kinetic parameters of the reaction were calculated using finite element dynamics (FED) and NEB methods. The steady-state current-potential curves and the distributions of CO and HCOOH concentrations were presented in Fig. S45 in the ESM, Figs. 4(e) and 4(f), respectively. The results show that the absence of dual-hydroxyl groups would result in the decrease of CO and HCOOH concentrations, indicating the significance of dual-hydroxyl groups for the improvement of activity. Moreover, from the concentration distribution plots of CO and HCOOH in Dha-COF-Co, it can be observed that CO$_2$RR primarily occurs at the porphyrin-Co site, while MOR partially happens at the dual-hydroxyl group site. The result is consistent with the above results. Furthermore, we discover that the products generated from porphyrin-Co in MOR are relatively narrow in the corners that might hinder the mass transfer. The introduction of dual-hydroxyl unit in Dha-COF-Co can serve as auxiliary to largely improve the kinetics of MOR, which is consistent with the superior performance of Dha-COF-Co to Naph-COF-Co.

## 4   Conclusions

In summary, we give insight into the inherent nature of the retrenchment of EC by exploring the photo-electrocatalytic MOR-CO$_2$RR coupling system using a kind of hydroxyl-rich COFs (Dha-COF-Co) with well-tuned pore structure and morphology. Specifically, an overall EC retrenchment of ~41.2% (highest in porous crystalline materials) can be achieved when replacing the anodic OER by MOR in the photo-electrocatalytic MOR coupled with CO$_2$RR system, which can give FE$_{HCOOH}$ (anode, ~100%) and FE$_{CO}$ (cathode, >95%) at 1.8 V. In addition, the crucial role of

hydroxyl functional group is systematically studied through different *in-situ/ex-situ* characterizations and DFT calculations, in which the hydroxyl can act as auxiliary catalytic site to facilitate mass transfer and promote $H_2O$ dissociation to boost the overall reaction kinetics and EC retrenchment for $CO_2$ coupling electrocatalytic systems. The design of such powerful COFs based electrocatalysts would be an effective strategy to lower EC and enhance energy efficiency for the advanced $CO_2RR$ coupling system.

## Acknowledgements

**Electronic Supplementary Material** Supplementary material (further details of synthesis; materials characterizations; XRD patterns; additional SEM, TEM images; XPS spectra and electrochemical characterizations) is available in the online version of this article at https://doi.org/10.26599/NRE.2024.9120146.

## Declaration of conflicting interests

The authors declare no conflicting interests regarding the content of this article.

## Data availability

All data needed to support the conclusions in the paper are presented in the manuscript and/or the Supplementary Materials. Additional data related to this paper may be requested from the corresponding author upon request.

## Author contributions

Y.-Q. L. and Y.-R. W. conceived and designed the idea. Y.-R. W. H.-M. D. and M. Y. designed the experiments, collected and analyzed the data. Q. L., J.-W. S., Q. H., J. Z. and S.-L. L. assisted with the experiments and characterizations. Y.-R. W. wrote the manuscript. Y.-R. W., Y. Z., Y. C. and Y.-Q. L. discussed the results and prepared the manuscript. All the authors reviewed and contributed to this paper.

## References

[1] Wakerley, D.; Lamaison, S.; Wicks, J.; Clemens, A.; Feaster, J.; Corral, D.; Jaffer, S. A.; Sarkar, A.; Fontecave, M.; Duoss, E. B. et al. Gas diffusion electrodes, reactor designs and key metrics of low-temperature $CO_2$ electrolysers. *Nat. Energy* **2022**, *7*, 130–143.

[2] Peng, X. Y.; Zeng, L. B.; Wang, D. S.; Liu, Z. B.; Li, Y.; Li, Z. J.; Yang, B.; Lei, L. C.; Dai, L. M.; Hou, Y. Electrochemical C–N coupling of $CO_2$ and nitrogenous small molecules for the electrosynthesis of organonitrogen compounds. *Chem. Soc. Rev.* **2023**, *52*, 2193–2237.

[3] Cai, T.; Sun, H. B.; Qiao, J.; Zhu, L. L.; Zhang, F.; Zhang, J.; Tang, Z. J.; Wei, X. L.; Yang, J.; Yuan, Q. Q. et al. Cell-free chemoenzymatic starch synthesis from carbon dioxide. *Science* **2021**, *373*, 1523–1527.

[4] Kim, J. Y. T.; Zhu, P.; Chen, F. Y.; Wu, Z. Y.; Cullen, D. A.; Wang, H. T. Recovering carbon losses in $CO_2$ electrolysis using a solid electrolyte reactor. *Nat. Catal.* **2022**, *5*, 288–299.

[5] Masel, R. I.; Liu, Z. C.; Yang, H. Z.; Kaczur, J. J.; Carrillo, D.; Ren, S. X.; Salvatore, D.; Berlinguette, C. P. An industrial perspective on catalysts for low-temperature $CO_2$ electrolysis. *Nat. Nanotechnol.* **2021**, *16*, 118–128.

[6] Ma, W. C.; He, X. Y.; Wang, W.; Xie, S. J.; Zhang, Q. H.; Wang, Y. Electrocatalytic reduction of $CO_2$ and CO to multi-carbon compounds over Cu-based catalysts. *Chem. Soc. Rev.* **2021**, *50*, 12897–12914.

[7] Huang, L.; Gao, G.; Yang, C. B.; Li, X. Y.; Miao, R. K.; Xue, Y. R.; Xie, K.; Ou, P. F.; Yavuz, C. T.; Han, Y. et al. Pressure dependence in aqueous-based electrochemical $CO_2$ reduction. *Nat. Commun.* **2023**, *14*, 2958.

[8] Hao, Y. N.; Hu, F.; Zhu, S. Q.; Sun, Y. J.; Wang, H.; Wang, L. Q.; Wang, Y.; Xue, J. J.; Liao, Y. F.; Shao, M. H. et al. MXene-regulated metal-oxide interfaces with modified intermediate configurations realizing nearly 100% $CO_2$ electrocatalytic conversion. *Angew. Chem., Int. Ed.* **2023**, *62*, e202304179.

[9] Liu, M. H.; Yang, S.; Yang, X. B.; Cui, C. X.; Liu, G. J.; Li, X. W.; He, J.; Chen, G. Z.; Xu, G. Zeng, G. F. Post-synthetic modification of covalent organic frameworks for $CO_2$ electroreduction. *Nat. Commun.* **2023**, *14*, 3800.

[10] Ma, X. D.; Xu, L.; Liu, S. J.; Zhang, L. B.; Tan, X. X.; Wu, L. M.; Feng, J. Q.; Liu, Z. M.; Sun, X. F.; Han, B. X. Electrochemical C–C coupling between $CO_2$ and formaldehyde into ethanol. *Chem Catal.* **2022**, *2*, 3207–3224.

[11] Li, H. B.; Jiang, Y. L.; Li, X. Y.; Davey, K.; Zheng, Y.; Jiao, Y.; Qiao, S. Z. $C_{2+}$ selectivity for $CO_2$ electroreduction on oxidized Cu-based catalysts. *J. Am. Chem. Soc.* **2023**, *145*, 14335–14344.

[12] Zeng, L.; Yang, Q. H.; Wang, J. X.; Wang, X.; Wang, P. J.; Wang, S. C.; Lv, S. D.; Muhammad, S.; Liu, Y. C.; Yi, H. et al. Programmed alternating current optimization of Cu-catalyzed C–H bond transformations. *Science* **2024**, *385*, 216–223.

[13] Zeng, L.; Li, H. R.; Hu, J. C.; Zhang, D. C.; Hu, J. Y.; Peng, P.; Wang, S. C.; Shi, R. Y.; Peng, J. Q.; Pao, C. W. et al. Electrochemical oxidative aminocarbonylation of terminal alkynes. *Nat. Catal.* **2020**, *3*, 438–445.

[14] Li, R.; Xiang, K.; Peng, Z. K.; Zou, Y. Q.; Wang, S. Y. Recent advances on electrolysis for simultaneous generation of valuable chemicals at both anode and cathode. *Adv. Energy Mater.* **2021**, *11*, 2102292.

[15] Fan, L. F.; Ji, Y. X.; Wang, G. X.; Chen, J. X.; Chen, K.; Liu, X.; Wen, Z. H. High entropy alloy electrocatalytic electrode toward alkaline glycerol valorization coupling with acidic hydrogen production. *J. Am. Chem. Soc.* **2022**, *144*, 7224–7235.

[16] Zhao, X.; Du, L. J.; You, B.; Sun, Y. J. Integrated design for electrocatalytic carbon dioxide reduction. *Catal. Sci. Technol.* **2020**, *10*, 2711–2720.

[17] Tang, C.; Zhang, R.; Lu, W. B.; Wang, Z.; Liu, D. N.; Hao, S.; Du, G.; Asiri, A. M.; Sun, X. P. Energy-saving electrolytic hydrogen generation: $Ni_2P$ nanoarray as a high-performance non-noble-metal electrocatalyst. *Angew. Chem., Int. Ed.* **2017**, *56*, 842–846.

[18] Zhou, Q. W.; Shen, Z. H.; Zhu, C.; Li, J. C.; Ding, Z. Y.; Wang, P.; Pan, F.; Zhang, Z. Y.; Ma, H. X.; Wang, S. Y. et al. Nitrogen-doped CoP electrocatalysts for coupled hydrogen evolution and sulfur generation with low energy consumption. *Adv. Mater.* **2018**, *30*, 1800140.

[19] Yan, D. F.; Mebrahtu, C.; Wang, S. Y.; Palkovits, R. Innovative electrochemical strategies for hydrogen production: From electricity input to electricity output. *Angew. Chem., Int. Ed.* **2023**, *62*, e202214333.

[20] Deng, C.; Toe, C. Y.; Li, X.; Tan, J. J.; Yang, H. P.; Hu, Q.; He, C. X. Earth-abundant metal-based electrocatalysts promoted anodic reaction in hybrid water electrolysis for efficient hydrogen

production: Recent progress and perspectives. *Adv. Energy Mater.* **2022**, *12*, 2201047.

[21] Wang, J. H.; Wang, S. C.; Wei, Z. H.; Wang, P. J.; Cao, Y. W.; Huang, Y.; He, L.; Lei, A. W. Synchronous recognition of amines in oxidative carbonylation toward unsymmetrical ureas. *Science* **2024**, *386*, 776–782.

[22] Bu, F. X.; Deng, Y. Q.; Xu, J.; Yang, D. L.; Li, Y.; Li, W.; Lei, A. W. Electrocatalytic reductive deuteration of arenes and heteroarenes. *Nature* **2024**, *634*, 592–599.

[23] Verma, S.; Lu, S.; Kenis, P. J. A. Co-electrolysis of CO₂ and glycerol as a pathway to carbon chemicals with improved technoeconomics due to low electricity consumption. *Nat. Energy* **2019**, *4*, 466–474.

[24] Chen, Z. J.; Dong, J. Y.; Wu, J. J.; Shao, Q. T.; Luo, N.; Xu, M. W.; Sun, Y. M.; Tang, Y. B.; Peng, J.; Cheng, H. M. Acidic enol electrooxidation-coupled hydrogen production with ampere-level current density. *Nat. Commun.* **2023**, *14*, 4210.

[25] Fan, L.; Bai, X. W.; Xia, C.; Zhang, X.; Zhao, X. H.; Xia, Y.; Wu, Z. Y.; Lu, Y. Y.; Liu, Y. Y.; Wang, H. T. CO₂/carbonate-mediated electrochemical water oxidation to hydrogen peroxide. *Nat. Commun.* **2022**, *13*, 2668.

[26] Zhu, Y.; Zhang, J. H.; Qian, Q. Z.; Li, Y. P.; Li, Z. Y.; Liu, Y.; Xiao, C.; Zhang, G. Q.; Xie, Y. Dual nanoislands on Ni/C hybrid nanosheet activate superior hydrazine oxidation-assisted high-efficiency H₂ production. *Angew. Chem., Int. Ed.* **2022**, *61*, e202113082.

[27] van der Ham, M. P. J. M. ; van Keulen, E.; Koper, M. T. M.; Tashvigh, A. A.; Bitter, J. H. Steering the selectivity of electrocatalytic glucose oxidation by the Pt oxidation state. *Angew. Chem., Int. Ed.* **2023**, *62*, e202306701.

[28] Huang, B.; Ge, Y. Y.; Zhang, A.; Zhu, S. Q.; Chen, B.; Li, G. X.; Yun, Q. B.; Huang, Z. Q.; Shi, Z. Y.; Zhou, X. C. et al. Seeded synthesis of hollow PdSn intermetallic nanomaterials for highly efficient electrocatalytic glycerol oxidation. *Adv. Mater.* **2023**, *35*, 2302233.

[29] Lu, Y. X.; Liu, T. Y.; Dong, C. L.; Yang, C. M.; Zhou, L.; Huang, Y. C.; Li, Y. F.; Zhou, B.; Zou, Y. Q.; Wang, S. Y. Tailoring competitive adsorption sites by oxygen-vacancy on cobalt oxides to enhance the electrooxidation of biomass. *Adv. Mater.* **2022**, *34*, 2107185.

[30] Feng, C.; Lyu, M. Y.; Shao, J. X.; Wu, H. Y.; Zhou, W. L.; Qi, S.; Deng, C.; Chai, X. Y.; Yang, H. P.; Hu, Q. et al. Lattice strain engineering of Ni₂P enables efficient catalytic hydrazine oxidation-assisted hydrogen production. *Adv. Mater.* **2023**, *35*, 2305598.

[31] Han, G. Q.; Li, G. D.; Sun, Y. J. Electrocatalytic dual hydrogenation of organic substrates with a Faradaic efficiency approaching 200%. *Nat. Catal.* **2023**, *6*, 224–233.

[32] Li, Y. H.; Ozden, A.; Leow, W. R.; Ou, P. F.; Huang, J. E.; Wang, Y. H.; Bertens, K.; Xu, Y.; Liu, Y.; Roy, C. et al. Redox-mediated electrosynthesis of ethylene oxide from CO₂ and water. *Nat. Catal.* **2022**, *5*, 185–192.

[33] Wei, X. F.; Li, Y.; Chen, L. S.; Shi, J. L. Formic acid electro-synthesis by concurrent cathodic CO₂ reduction and anodic CH₃OH oxidation. *Angew. Chem., Int. Ed.* **2021**, *60*, 3148–3155.

[34] Sun, S. N.; Dong, L. Z.; Li, J. R.; Shi, J. W.; Liu, J.; Wang, Y. R.; Huang, Q.; Lan, Y. Q. Redox-active crystalline coordination catalyst for hybrid electrocatalytic methanol oxidation and CO₂ reduction. *Angew. Chem., Int. Ed.* **2022**, *61*, e202207282.

[35] Hao, J.; Liu, J. W.; Wu, D.; Chen, M. X.; Liang, Y.; Wang, Q.; Wang, L.; Fu, X. Z.; Luo, J. L. *In situ* facile fabrication of Ni(OH)₂ nanosheet arrays for electrocatalytic co-production of formate and hydrogen from methanol in alkaline solution. *Appl. Catal. B: Environ.* **2021**, *281*, 119510.

[36] Li, J. S.; Wei, R. L.; Wang, X.; Zuo, Y.; Han, X.; Arbiol, J.; Llorca, J.; Yang, Y. Y.; Cabot, A.; Cui, C. H. Selective methanol-to-formate electrocatalytic conversion on branched nickel carbide. *Angew. Chem., Int. Ed.* **2020**, *59*, 20826–20830.

[37] Ma, Y. B.; Zhou, Y. Y.; Wang, C. L.; Gao, B.; Li, J. L.; Zhu, M.; Wu, H.; Zhang, C.; Qin, Y. Q. Photothermal-magnetic synergistic effects in an electrocatalyst for efficient water splitting under optical-magnetic fields. *Adv. Mater.* **2023**, *35*, 2303741.

[38] Kumaravel, V.; Bartlett, J.; Pillai, S. C. Photoelectrochemical conversion of carbon dioxide (CO₂) into fuels and value-added products. *ACS Energy Lett.* **2020**, *5*, 486–519.

[39] Deng, X.; Li, R.; Wu, S. K.; Wang, L.; Hu, J. H.; Ma, J.; Jiang, W. B.; Zhang, N.; Zheng, X. S.; Gao, C. et al. Metal-organic framework coating enhances the performance of Cu₂O in photoelectrochemical CO₂ reduction. *J. Am. Chem. Soc.* **2019**, *141*, 10924–10929.

[40] Moazzami, N.; Khadempir, S.; Karimi-Maleh, H.; Karimi, F.; Karaman, C. Enhanced methanol electrooxidation by electroactivated Pd/Ni(OH)₂/N–rGO catalyst. *Int. J. Hydrogen Energy* **2023**, *48*, 6680–6690.

[41] Dubale, A. A.; Zheng, Y. Y.; Wang, H. L.; Hübner, R.; Li, Y.; Yang, J.; Zhang, J. W.; Sethi, N. K.; He, L. Q.; Zheng, Z. K. et al. High-performance bismuth-doped nickel aerogel electrocatalyst for the methanol oxidation reaction. *Angew. Chem., Int. Ed.* **2020**, *59*, 13891–13899.

[42] Wang, Y. R.; Ding, H. M.; Sun, S. N.; Shi, J. W.; Yang, Y. L.; Li, Q.; Chen, Y. F.; Li, S. L.; Lan, Y. Q. Light, heat and electricity integrated energy conversion system: Photothermal-assisted Co-electrolysis of CO₂ and methanol. *Angew. Chem., Int. Ed.* **2022**, *61*, e202212162.

[43] Lu, M.; Zhang, M.; Liu, J.; Chen, Y. F.; Liao, J. P.; Yang, M. Y.; Cai, Y. P.; Li, S. L.; Lan, Y. Q. Covalent organic framework based functional materials: Important catalysts for efficient CO₂ utilization. *Angew. Chem., Int. Ed.* **2022**, *61*, e202200003.

[44] Liu, R. Y.; Tan, K. T.; Gong, Y. F.; Chen, Y. Z.; Li, Z. E.; Xie, S. L.; He, T.; Lu, Z.; Yang, H.; Jiang, D. L. Covalent organic frameworks: An ideal platform for designing ordered materials and advanced applications. *Chem. Soc. Rev.* **2021**, *50*, 120–242.

[45] Wang, D. G.; Qiu, T. J.; Guo, W. H.; Liang, Z. B.; Tabassum, H.; Xia, D. G.; Zou, R. Q. Covalent organic framework-based materials for energy applications. *Energy Environ. Sci.* **2021**, *14*, 688–728.

[46] Wang, Y. R.; Ding, H. M.; Ma, X. Y.; Liu, M.; Yang, Y. L.; Chen, Y. F.; Li, S. L.; Lan, Y. Q. Imparting CO₂ electroreduction auxiliary for integrated morphology tuning and performance boosting in a porphyrin-based covalent organic framework. *Angew. Chem., Int. Ed.* **2022**, *61*, e202114648.

[47] Zhao, Y. W.; Wang, J. N.; Pei, R. J. Micron-sized ultrathin metal-organic framework sheet. *J. Am. Chem. Soc.* **2020**, *142*, 10331–10336.

[48] Hernan, L.; Morales, J.; Sanchez, L.; Tirado, J. L.; Espinos, J. P.; Gonzalez Elipe, A. R. Diffraction and XPS studies of misfit layer chalcogenides intercalated with cobaltocene. *Chem. Mater.* **1995**, *7*, 1576–1582.

[49] Shen, F. C.; Sun, S. N.; Xin, Z. F.; Li, S. L.; Dong, L. Z.; Huang, Q.; Wang, Y. R.; Liu, J.; Lan, Y. Q. Hierarchically phosphorus doped bimetallic nitrides arrays with unique interfaces for efficient water splitting. *Appl. Catal. B: Environ.* **2019**, *243*, 470–480.

[50] Wang, X. P.; Xi, S. B.; Lee, W. S. V.; Huang, P. R.; Cui, P.; Zhao, L.; Hao, W. C.; Zhao, X. S.; Wang, Z. B.; Wu, H. J. et al. Materializing efficient methanol oxidation via electron delocalization in nickel hydroxide nanoribbon. *Nat. Commun.* **2020**, *11*, 4647.

[51] Yi, J. D.; Xie, R. K.; Xie, Z. L.; Chai, G. L.; Liu, T. F.; Chen, R. P.; Huang, Y. B.; Cao, R. Highly selective CO₂ electroreduction to CH₄ by *in situ* generated Cu₂O single-type sites on a conductive MOF: Stabilizing key intermediates with hydrogen bonding. *Angew. Chem., Int. Ed.* **2020**, *59*, 23641–23648.

[52] Strmcnik, D.; Uchimura, M.; Wang, C.; Subbaraman, R.; Danilovic, N. ; van der Vliet, D.; Paulikas, A. P.; Stamenkovic, V. R.; Markovic, N. M. Improving the hydrogen oxidation reaction rate by promotion of hydroxyl adsorption. *Nat. Chem.* **2013**, *5*, 300–306.

**Yi-Rong Wang** received her M.S. degree (2019) and Ph.D. degrees (2022) from Nanjing Normal University under the supervision of Prof. Ya-Qian Lan. Since 2022, she has carried out postdoctoral research at South China Normal University with Prof. Ya-Qian Lan. Her current research focuses on the synthesis of crystalline porous materials (MOF- and COF-based composites) and their applications in energy storage and conversion.

**Hui-Min Ding** received her undergraduate degree (2019) and M.S. degree (2023) at Shandong Liaocheng University and Nanjing Normal University. Her research focuses on the design and synthesis of highly efficient MOF-based hybrid electrocatalysts for electrocatalytic reduction of carbon dioxide.

**Ming Yue** received her B.Eng. degree at East China University of Science and Technology in 2021, and is now studying for a postgraduate degree at South China Normal University under the supervision of Prof. Ya-Qian Lan. Her research interest focuses on the design and synthesis of crystalline porous materials (MOF- and COF-based composites) for energy conversion.

**Ying Zang** received her Ph.D. in 2021 from Zhengzhou University, under the supervision of Prof. Thomas C. W. Mak. Since 2021, she has carried out postdoctoral research at South China Normal University with Prof. Ya-Qian Lan. Her current research interests focus on crystalline functional materials (COFs- and MOFs- based composites), as well as their application in photocatalysis, electrocatalysis, energy storage, and conversion.

**Yifa Chen** received his B.S. degree from School of Chemistry, Beijing Institute of Technology. He subsequently obtained his Ph.D. degree from School of Chemistry and Chemical Engineering, Beijing Institute of Technology under the supervision of Prof. Bo Wang. In 2022, he joined South China Normal University (SCNU, China) as a professor of chemistry. His research interest focuses on the fabrication of porous crystalline material based devices like membranes, foams and fibers that can be applicable in energy storage, environment treatment or photo-/electro-catalysis.

**Ya-Qian Lan** received his B.S. and Ph.D. degrees (2009) from Northeast Normal University under the supervision of Prof. Zhong-Min Su. In 2010, he joined the National Institute of Advanced Industrial Science and Technology (AIST, Japan) as a JSPS postdoctoral fellow. In 2012, he became a professor of chemistry at Nanjing Normal University (NNU, China). In 2021, he joined South China Normal University (SCNU, China) as a professor of chemistry. His current research interest focuses on the synthesis of new crystalline materials and catalytic research related to clean energy applications.